NUMERICAL SIMULATION OF SLD ICE ACCRETIONS

J.M. Hospers, H.W.M. Hoeijmakers
University of Twente, Enschede, the Netherlands

Abstract

In this study, computational methods are presented that compute ice accretion on multiple-element airfoils in specified icing conditions. The "Droplerian" numerical simulation method used is based on an Eulerian method for predicting droplet trajectories and the resulting droplet catching efficiency on the surface of the configuration. Flow field and droplet catching efficiency form input for Messinger's model for ice accretion. The droplet trajectory method has been constructed such that the solution of any flow-field simulation (e.g. potential-flow, Euler equations) can be used as input for the finite-volume solution method. On an unstructured grid the spatial distribution of droplet loading and droplet velocity are obtained. From these quantities the droplet catching efficiency is derived. Of special interest in this study are the Supercooled Large Droplets (SLD). The simulation of SLD's requires a specific splashing model.

For a single-element airfoil a good agreement is found with the Lagrangian method 2DFOIL-ICE and with experimental results. The comparison of the catching efficiency predicted by both simulation methods is good for the smaller droplets. For larger (SLD) droplets the splashing model is a significant improvement to the catching efficiency results when compared with the experimental results.

1 Introduction

Aircraft icing has long been recognized as a serious flight safety problem. According to [11], in the period 1992–2000, airframe icing was involved in more than 50 accidents and incidents, claiming more than 800 lives, in the US alone. Icing occurs when super-cooled water droplets hit the aircraft in-flight, at a level where the temperature is at or below the freezing point. Ice accretion on the wing leading edge or on the tail plane can result in non-aerodynamic shapes. This results in serious degradation of the aerodynamic performance, such as an increase in drag, altered handling characteristics and a decrease in maximum lift, therewith an increase in minimum flight speed. Also, ice accretion on parts of the engine nacelles or on propellers can cause dangerous situations. Computer simulation of the ice accretion process provides an attractive method for determining the ice shapes on aircraft wings and evaluating icing for a wide range of icing conditions. An ice accretion model that accurately predicts growth shapes on an arbitrary airfoil is valuable for analysis of the sensitivity of airfoils to ice accretion and for analysis of the influence of variables such as airspeed and angle of attack, pressure, temperature, humidity and droplet size on the accretion process. The predicted ice shapes can be used in wind tunnel and flight tests to assess degradation of aircraft performance and handling qualities in icing conditions.

The same model can also be used to assess the energy requirements necessary to prevent ice build-up on an airfoil. Once a model has been validated, it will provide a cost effective means of performing most of the icing research studies which now rely upon experimental techniques.

Nowadays, it is common practice in the aircraft manufacturing industry to apply computational methods for ice accretion prediction in two-dimensional flows. Studies to extend

the two-dimensional ice growth model to three-dimensional flows are in progress at for example NASA GRC as well as at CIRA and ONERA. The 2DFOIL-ICE method [12, 13, 2, 3, 5] predicts the growth of ice on 2D surfaces. It is based on a quasi-steady model that takes into account all important mass and heat transfer processes that occur when super-cooled water droplets strike an airfoil. The droplets either freeze immediately upon impact or freeze partly while the rest of the water runs back on the airfoil. The capabilities of the method have recently been extended by the inclusion of a model for thermal ice protection systems [2]. The use of this method, therefore, not only enables the assessment of potential icing hazards due to ice growth on unprotected surfaces but also the design and appropriate placement of thermal ice protection systems.

Aircraft icing is a threat during take-off and landing, when high-lift devices of the multi-element airfoil are deployed. The geometric capability of the method has recently been extended to the case of multi-element airfoil sections [5].

The objective of the present work is to compare numerical results and experimental data available from literature to the results obtained with Droplerian, focussing on the catching efficiency results, in order to assess its value as an analysis tool for carrying out more studies to further elucidate the pertinent physical phenomena involved in the ice accretion and anti-icing process.

A brief review of the ice accretion process is first presented. Followed by an introduction of supercooled large droplets. Then, the Eulerian droplet tracking procedure is explained. Next, comparisons with other numerical results and experimental data are made. Finally, some conclusions are presented.

2   Ice Accretion

The ice accretion process is a process involving several steps. When an aircraft flies through a cloud, supercooled droplets impinge on the surface of the aircraft due to the forward velocity of the aircraft. The trajectory that a droplet follows, and therefore the location at which it will impact

the surface, depends mostly on the droplet size, as it is determined mostly by the drag force on the droplet. Because the droplets are supercooled a mass of ice will form almost instantly at the moment the droplets contact the aircraft surface.

The size, shape and location of the ice accretion that will form depends on:

- The environmental parameters, e.g. ambient air temperature, pressure, cloud liquid water content (LWC), relative humidity and median volumetric diameter (MVD).

- The aircraft surface conditions, e.g. surface temperature, roughness and surface tension at the air/water interface.

- The flow parameters, e.g. flight velocity, angle of attack and icing time.

2.1   Types of ice accretion

Two distinct types of ice accretion have been observed:

Rime-ice accretions A dry, opaque and milky-white ice deposit with a density lower than that of the water in the impinging droplets. It usually occurs at low airspeeds, lower temperatures and lower LWC's. In rime ice conditions the released latent heat of freezing is insufficient to raise the local temperature above the freezing point and all the water in the impinging droplet freezes fully upon impact. Generally, rime-ice accretions have a streamlined shape.

Glaze-ice accretions A heavy coating of a transparent ice which spreads over the wing and has a density close to that of the water in the impinging droplets. It usually develops at higher airspeeds, temperatures closer to the freezing point and higher LWC's. In glaze-ice conditions, due to the relatively high amount of released latent heat of freezing, the temperature increases to $0\,°C$. Only part of the water in the droplets freezes upon impact, the rest of the water runs back along

the airfoil surface. This run-back water often freezes further downstream on the airfoil surface. Generally, the ice formations have an irregular, non-aerodynamic shape which may jeopardize the aerodynamic characteristics of the airfoil section.

3 Supercooled Large Droplets

Since the crash of an ATR-72 at Roselawn, Indiana in 1994, scientific interest in the phenomenon of Supercooled Large Droplets (SLD) has increased. SLD are defined as droplets with a:

- Temperature below freezing ($T < 0\,°C$)

- Diameter larger than normal droplets ($d > 50\,\mu m$)

These SLD are thought to be the main cause of this and several other aviation incidents. Because of their size SLD present specific problems:

- Ice accretion occurs faster than for normal droplets.

- Ice accretion occurs at different locations than where normal droplet ice accretion occurs.

- Ice accretion is harder to predict than for normal droplets.

Sometimes, droplets with sizes up to 1 mm are reported, which is much larger than the largest diameter (50 µm) prescribed in the FAA CFR Appendix C flight envelope.

A new flight envelope is being developed, known as "Appendix X", including SLD-conditions. In preparation of these new regulations the industry wants to improve their understanding and predictive capabilities of SLD specific ice accretions. The present research focusses on the prediction of SLD trajectories and the corresponding impingement distribution on airfoils.

3.1 Analysis of Droplet Forces

Because of the size of SLD it is unknown whether or not the conventional assumptions made for trajectory calculations are valid. For normal droplets,

it is common to assume that all forces besides drag, gravity and buoyancy can be ignored. To assess if this is a valid assumption for the larger SLD an analysis of two different sets of trajectories has been performed. One set of trajectories has been calculated using the conventional assumption (only drag, gravity and buoyancy) and the other set was calculated using a number of additional forces. The set of "all" forces consists of:

- Drag

- Gravity

- Buoyancy

- Basset history force

- Virtual mass force

The full force on a droplet contains even more force-terms, some of which are unknown. There are some lift terms, e.g. the Saffman lift force, but these depend on rotation. Since for most calculations the potential-flow-equations are used, which assume that rotation is not present, these terms are ignored. The specifications for the forces were taken from work of van Eijkeren [15]:

3.1.1 Drag Force

The drag force is accounted for using following formulation:

$$\vec{f}_D = \frac{\vec{D}}{\rho_w V_d} = \frac{\rho_a \left| \vec{U}_a - \vec{U}_d \right| \left(\vec{U}_a - \vec{U}_d \right) A_d C_D}{2\rho_w V_d} \tag{1}$$

where C_D is usually a function of the Reynolds number based on the relative droplet velocity Re_d:

$$Re_d \equiv \frac{\rho_a \left| \vec{U}_a - \vec{U}_d \right| d}{\mu_a} \tag{2}$$

The expression for the drag coefficient can range from an expression for small diameter droplets to special relations for deforming droplets (SLD diameter droplets). In the current model C_D is derived from [8]:

$$\frac{C_D Re_d}{24} = 1 + 0.0197 Re_d^{0.63} + 2.6 \cdot 10^{-4} Re_d^{1.38} \tag{3}$$

which is valid for $Re_d < 1000$.

3.1.2 Gravity Force

In most conventional models the gravity is combined with at least part of the buoyancy. For this study the two have been separated. The gravity force consists only of the force acting on the droplet by gravitational acceleration:

$$\vec{f}_g = \rho_w V_d \vec{g} \tag{4}$$

3.1.3 Buoyancy Force

The buoyancy force is caused by a pressure gradient. In most common methods, only the constant pressure gradient caused by the constant gravity field is taken into account, resulting in:

$$\vec{f}_b = -\rho_a V_d \vec{g} \tag{5}$$

However, for the present analysis the pressure gradient also takes into account the local pressure gradient induced by the flow field.

$$\vec{f}_b = -V_d \vec{\nabla} p \tag{6}$$

3.1.4 Basset History Force

Perhaps the most important question is whether or not the Basset history force has to be accounted for. This term is based on the relative speed at which the boundary layer adapts to changes in the surrounding flow. Calculation of this term is particularly complicated because it involves a time-integration over the path of the droplet.

$$\vec{f}_B = -3d\mu_a \pi \int\limits_{-\infty}^{t} K(t-\tau, \tau) \frac{d\left(\vec{U} - \vec{U}_d\right)}{dt} d\tau \tag{7}$$

where the kernel K has been chosen as the kernel for non-creeping flow conditions as [9]:

$$K(t-\tau, \tau) = \left[\left(\frac{4\pi(t-\tau)}{\tau_d}\right)^{0.2} + \left(\frac{\pi(t-\tau)^2}{f_H^3 \tau_d^2} \mathrm{Re}_d^3\right)^{0.4}\right]^{-2.5} \tag{8}$$

with $\tau_d = \frac{\rho_a d^2}{\mu_a}$ and $f_H = 0.75 + 0.2\mathrm{Re}_d$

3.1.5 Virtual Mass Force

The virtual mass force is based on the acceleration of the air surrounding the droplets. Accelerating a droplet means that the air surrounding it has to accelerate as well. The virtual mass force therefore depends on the relative acceleration:

$$\vec{f}_{vm} = \frac{1}{2}\rho_a V_d \left(\frac{d\vec{U}}{dt} - \frac{d\vec{U}_d}{dt}\right) \tag{9}$$

3.1.6 Results

Both calculation sets were performed for two droplet sizes. These droplet sizes chosen are the minimum and maximum droplet diameters from the 10-bin droplet distribution determined in an impingement experiment performed by Papadakis [10]: 16 μm and 1046 μm, respectively. The same experiment is used in section 5 to validate the Eulerian droplet impingement model discussed in section 4. The considered configuration is a NACA-23012 airfoil at 2.5°angle of attack. For this configuration the impingement limits were determined and around 100 droplet trajectories were calculated within these limits.

The results are shown in Fig. 1. For each of the impinging trajectories the maximum of the force-components were determined, and only the trajectories corresponding to these maximum force-components were plotted. This corresponds to two or three different trajectories for each set of calculations. For both droplet sizes it can be concluded that the drag force is the dominant force, although the order of magnitude is almost 4 times larger for the larger droplets than it is for the smaller droplets. For the smaller droplets (Fig. 1a) the second most dominant force is the history force. However, it is already more than one order of magnitude smaller than the drag force. For the larger droplets (Fig. 1b) the buoyancy force becomes more important than the history force, the history force is again around one order of magnitude smaller than the dominant drag force.

The history force term is very time-consuming to calculate, since it involves integration over the entire time-domain up to the considered time. Furthermore, the history force acts as an increase in
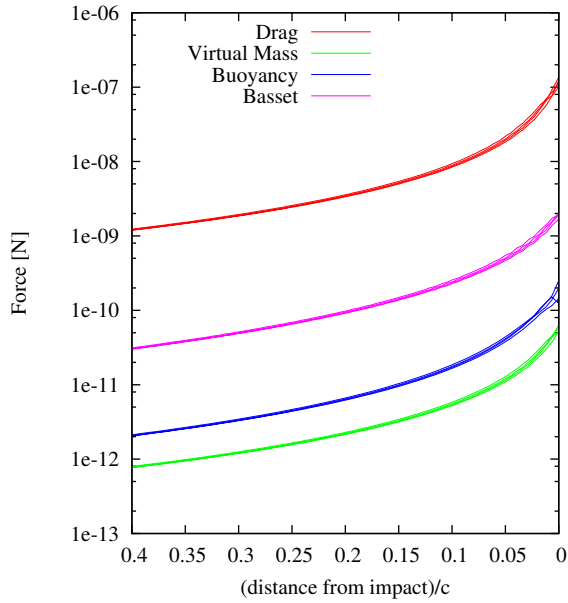
(a) Droplet diameter, $d = 16\,\mu m$
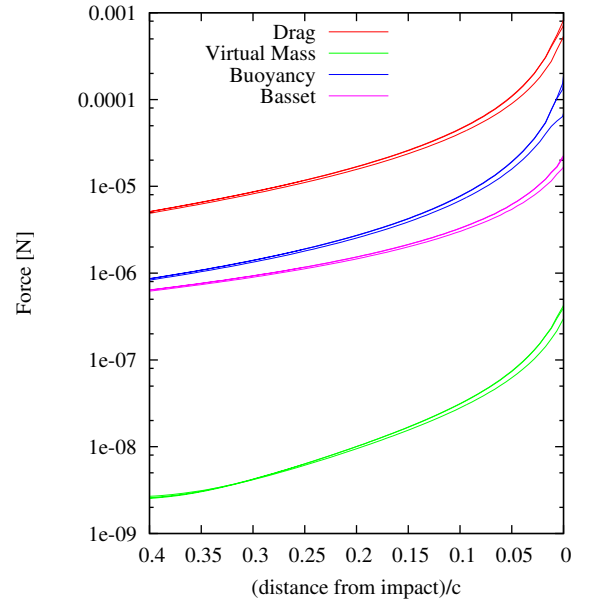
(b) Droplet diameter, $d = 1046\,\mu m$

Fig. 1 Magnitude of force components along droplet trajectories, only trajectories for which one of the components has a maximum value are shown

the drag. When ignoring the history force, part of the effects can be compensated by an increase in the drag force.

This gives reason to continue with the generally accepted method of including only drag, buoyancy and gravity. Including the history force would be very time consuming while the change in the droplet trajectories is minimal.

3.2 SLD Specific Model

A number of phenomena that are disregarded for normal ($< 50\,\mu m$) droplets are not readily disregarded for SLD because of their size. These phenomena may include:

- Splashing
- Rebound
- Breakup
- Deformation

According to [16] the only first-order effect is the effect of splashing. For now, the other effects (rebound, breakup and deformation) are ignored.
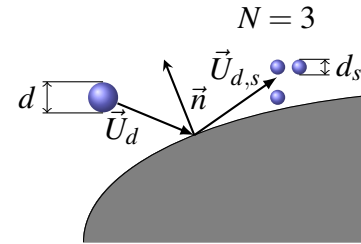
Fig. 2 Variables related to a splashing event

A sketch showing the relevant variables before and after the splashing event is shown in Fig. 2.

3.2.1 *Splashing Parameters*

The main parameters determining splashing behaviour are the droplet Weber-number (We) and the droplet Ohnesorge-number (Oh). The Weber-number is defined as:

$$\text{We}_n = \frac{\rho_a \left(\vec{U}_d \cdot \vec{n} \right)^2 d}{\sigma_d} \qquad (10)$$

where $\vec{U}_d \cdot \vec{n}$ is the component of the droplet velocity normal to the airfoil surface and σ_d is the

surface tension at the air/water interface. The Ohnesorge-number is defined as:

$$\text{Oh} = \frac{\mu_a}{\sqrt{\rho_a \sigma_d d}} = \frac{\sqrt{\text{We}_n}}{\text{Re}_{d,n}} \tag{11}$$

where $\text{Re}_{d,n}$ is the droplet Reynolds number based on the velocity component normal to the airfoil surface.

Various combinations of these two dimensionless-numbers are encountered in literature. Two main splashing parameters can be identified, the Cossali splashing parameter [1] defined as:

$$K = \text{Oh}^{-2/5}\text{We}_n \tag{12}$$

and the Yarin and Weiss splashing parameter [17] defined as:

$$K_y = \Lambda^{-3/8} \left(\text{Oh}^{-2/5}\text{We}_n \right)^{5/16}$$
$$= \left[\frac{3}{2} \left(\frac{LWC}{\rho_w} \right)^{1/3} \right]^{-3/8} \left(\text{Oh}^{-2/5}\text{We}_n \right)^{5/16} \tag{13}$$

The differences between K and K_y are the prefactor Λ, denoting the droplet frequency and the power $5/16$, which appear in the definition of K_y (Eq. 13).

Both splashing parameters increase with increasing diameter, making splashing more likely for SLD than for normal droplets. When the splashing parameter exceeds a critical value splashing will occur. For the Yarin and Weiss parameter this value was found to be

$$K_{y,crit} = 17 \tag{14}$$

3.2.2 Mass-Loss Coefficient

To account for the mass of the droplets that splash away from the airfoil surface the mass-loss coefficient (ϕ) is introduced. This approach was taken from an empirical splashing model of Trujillo et al.[14]. Honsek, Habashi and Aubé [4] calibrated the mass-loss equation specifically for SLD-conditions. The resulting mass-loss coefficient is defined as:

$$\phi\left(K_y\right) = \frac{3.8}{\sqrt{K_y}} \left(1 - \exp\left[-0.85\left(K_y - K_{y,crit}\right) \right] \right) \tag{15}$$
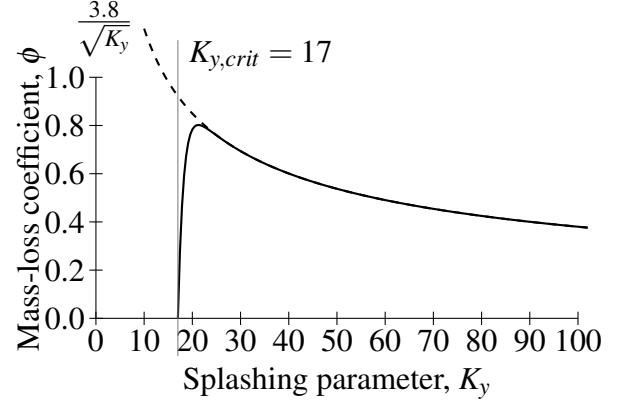
Fig. 3 Mass-loss coefficient according to Eq. 15

for $K_y \geq K_{y,crit} = 17$.

Equation 15 is illustrated in Fig. 3. Note that, within 1% accuracy, $\phi = \frac{3.8}{\sqrt{K_y}}$ for $K_y > 23$.

3.2.3 Secondary Droplets

The relation for the number of secondary droplets (N) is taken from Trujillo et al.'s original empirical model:

$$N = \frac{1}{22} \left(0.0437 \left[K \left(\frac{\left|\vec{U}_d\right|}{\vec{U}_d \cdot \vec{n}} \right)^2 - K_c \right] - 44.92 \right) \tag{16}$$

where K_c is the critical value for the Cossali splashing parameter, calculated from $K_{y,crit}$ (Eq. 14).

From the number of secondary droplets the average diameter (d_s) of the secondary droplets can be determined using mass-conservation:

$$d_s = \left(\frac{\phi}{N} \right)^{1/3} d \tag{17}$$

The average velocity of the secondary droplets ($\vec{U}_{d,s}$) follows again from Trujillo et al.:

$$\frac{\vec{U}_{d,s} \cdot \vec{t}}{\vec{U}_d \cdot \vec{t}} = 0.85 + 0.0025 \arctan\left(\frac{\vec{U}_d \cdot \vec{t}}{\vec{U}_d \cdot \vec{n}} \right) \tag{18a}$$

$$\frac{\vec{U}_{d,s} \cdot \vec{n}}{\vec{U}_d \cdot \vec{n}} = 0.12 + 0.002 \arctan\left(\frac{\vec{U}_d \cdot \vec{t}}{\vec{U}_d \cdot \vec{n}} \right) \tag{18b}$$

The secondary droplet velocity depends on the angle of impact of the droplets, in Eq. 18 the angle has been rewritten in terms of the normal and tangential velocity components for convenience.

4   Eulerian Droplet Tracking

Previously, droplet tracking was mostly performed in a Lagrangian frame. A single droplet was followed from a release point as it progressed in time. This means that, especially for multi-element airfoils, a large number of droplets had to be released. For every airfoil element the impingement limits (lower and upper) have to be found. When the limits are found the impingement distribution, i.e. the catching efficiency distribution, has to be determined within the upper and lower limit. This can mean that hundreds of droplet trajectories have to be computed. Furthermore, if the SLD effects discussed in the preceding section need to be implemented the entire structure and method of the existing computational method would have to be changed.

For these complicated geometries and SLD situations a droplet tracking method in an Eulerian frame has been developed. This means that a droplet velocity and droplet density distribution will be calculated on a computational grid, instead of following single droplets. One of the major advantages is that splashing effects can be implemented as a boundary condition on the airfoil surface.

The resulting droplet-flow equations are solved using a finite volume method based on work from Kelleners [6] and Koop [7]. The method employs unstructured grids and is currently applied to two-dimensional flows.

The method employs, similar to the Lagrangian method, only one-way-coupling. A flow field from any source can be used as input, as long as density, pressure and velocity components are provided.

The method is able to simulate both mono-disperse (i.e. only one diameter, the MVD) and multi-disperse droplet distributions. In case of multi-disperse distributions, the distribution is modeled as a series of bins, each representing an avarage diameter (d_i) and a fraction of the total LWC (f_i). For each bin the droplet model is solved seperately and a catching efficiency contribution β_i is computed for each of the bins. At the end of the droplet trajectory calculation the results for the droplet bins are combined. For a multi-disperse simulation with η bins the catching efficiency (β) would be:

$$\beta = \sum_{i=1}^{\eta} f_i \beta_i \qquad (19)$$

4.1   Governing Equations

Calculating the droplet density and droplet velocities in the entire domain leads to two conservation equations instead of the droplet equation of motion:

$$\frac{\partial \rho_d}{\partial t} + \vec{\nabla} \cdot \rho_d \vec{U}_d = 0 \qquad (20)$$

$$\frac{\partial \rho_d \vec{U}_d}{\partial t} + \vec{\nabla} \cdot \left(\rho_d \vec{U}_d \right) \vec{U}_d = \rho_d \vec{f}_D + \rho_d \left(1 - \frac{\rho_a}{\rho_w} \right) \vec{g} \qquad (21)$$

where the local droplet density (ρ_d) is the volume fraction of water contained in the droplets (α) multiplied with the local water density (ρ_w):

$$\rho_d = \alpha \rho_w \qquad (22)$$

the drag force per unit mass ($\vec{f}_D$) is the same drag force as in the Lagrangian method and in Eq. 1.

4.2   Boundary Conditions

To close the set of equations a number of boundary conditions is needed.

4.2.1   Inflow

The inflow boundary is chosen far upstream of the airfoil. At this point the droplet density is chosen to be equal to the cloud liquid water content, the droplet velocity is chosen equal to the free-stream air velocity.

$$\rho_d = LWC \qquad (23a)$$

$$\vec{U}_d = \vec{U}_\infty \qquad (23b)$$

4.2.2 Outflow

The outflow boundary condition is implemented by linearly extrapolating the value of ρ_d and $\vec{U}_d$ at the control point in a boundary cell to the ghost-cell outside the boundary.

4.2.3 Airfoil Surface

On the airfoil surface two boundary conditions can be imposed, depending on whether or not a flow of droplets into the airfoil is detected.

no inflow $\vec{U}_d \cdot \vec{n} \geq 0$:

No droplets can originate on the airfoil surface: $\rho_d = 0$. However, velocity is unaffected. $\vec{U}_d$ is linearly extrapolated from the value at the control point in a boundary cell.

inflow $\vec{U}_d \cdot \vec{n} < 0$:

Outflow boundary condition. Droplets are not influenced by the airfoil surface (other than through the aerodynamic drag). Both ρ_d and $\vec{U}_d$ are linearly extrapolated from their values at the control point in a boundary cell.

4.2.4 Re-Injection

Secondary droplets from a splashing event need to be re-injected into the droplet flow. This is done be appending to the boundary condition on the airfoil surface.

The splashed mass is equal to that of the mass-loss coefficient multiplied with the incoming mass:

$$M = \begin{cases} \phi \left(\rho_d \vec{U}_d \cdot \vec{n} \right) > 0 : & \text{Splashing} \\ 0 : & \text{No splashing} \end{cases} \quad (24)$$

The added momentum is equal to that of the mass-loss coefficient multiplied with the incoming momentum:

$$I = \begin{cases} \phi \left(\rho_d \vec{U}_d \cdot \vec{n} \right) \vec{U}_{d,s} = M \vec{U}_{d,s} : & \text{Splashing} \\ 0 : & \text{No splashing} \end{cases} \quad (25)$$

If a multi-disperse simulation is performed, the droplet-bin which is used for re-injection is
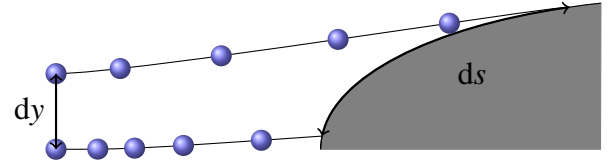
Fig. 4 Local catching efficiency for Lagrangian methods

chosen as the bin with the diameter closest to that of the secondary droplet diameter. This means that the average diameter of the simulated secondary droplets differs from the calculated average secondary droplet diameter from Eq. 17.

4.3 Catching Efficiency

The output from the droplet tracking method that is most important is the catching efficiency (sometimes also called collection efficiency). This variable, representing the dimensionless rate of mass of water depositing on the airfoil surface, determines for the most part the calculated ice accretion shape.

For a Lagrangian frame, the catching efficiency is defined as:

$$\beta = \frac{\mathrm{d}y}{\mathrm{d}s} \quad (26)$$

with $\mathrm{d}y$ and $\mathrm{d}s$ clarified in Fig. 4. This represents the mass-flux through a surface area $\mathrm{d}s$ on the airfoil, made dimensionless with the mass-flux far upstream. The mass of water between the two trajectories is assumed to remain constant.

For an Eulerian method, since individual droplet trajectories are not calculated, another method of calculating β will have to be found. Transfering Eq. 26 to an Eulerian frame the *local* mass-flux through the surface can be made dimensionless with the mass-flux far upstream, finding a *local* relation for β:

$$\beta = \frac{\rho_d \vec{U}_d \cdot \vec{n}}{LWC \left| \vec{U}_\infty \right|} \quad (27)$$

	20 μm MVD	236 μm MVD
AoA	2.5°	
c	0.9144 m	
LWC	0.19 g/m^3	1.89 g/m^3
$\left|\vec{U}_{a,\infty}\right|$	78.23 m/s	
T_∞	299 K	
p_∞	101330 Pa	

Table 1 Conditions for selected cases

5 Catching Efficiency Validation

In order to validate the Eulerian droplet tracking method a suitable test case was selected. Because of the availability of 2DFOIL-ICE, which calculates a potential-flow field using a panel-method, the results from the Eulerian droplet tracking method are compared to the results from 2DFOIL-ICE. This implies that the underlying flow field used for the Eulerian droplet tracking is also obtained from the potential-flow field as calculated by 2DFOIL-ICE. Besides this comparison between two computational results, a comparison with experimental impingement data of Papadakis et al. [10] has been performed.

5.1 Experimental Data

Experimental data is available through an experiment of Papadakis et al. [10]. They performed experiments with different MVD's for a NACA-23012 airfoil at 2.5° angle of attack (*AoA*). The impingement data is presented as a catching efficiency and the LWC distribution has been recorded so that it can be used in a multi-disperse simulation. Two cases were selected from the range of MVD's, the smallest and the largest MVD, to investigate the ability to predict both normal and SLD impingement regimes. The selected cases and the corresponding conditions are shown in Table 1.

For the experiment of Papadakis et al. the droplet distributions are given. These distributions can be used as input for the numerical simulations, which makes this experiment very suitable for validation purposes. Both 10-bin and 27-bin droplet distributions are provided. Since the difference

in the resulting catching efficiency is small, the 10-bin droplet distributions have been chosen for computational speed. The distributions for both MVD's are shown in Fig. 5.

5.2 Numerical Setup

The results from the Eulerian method, Droplerian, are compared to results from the Lagrangian method 2DFOIL-ICE. The Lagrangian method uses 400 panels in both the potential-flow simulation and the droplet tracking method. The mesh used for the Eulerian computation is shown in Fig. 6. A median dual mesh was generated, in which a control volume element was created for each vertex in the original triangular mesh. The mesh contains 27660 triangular elements.

5.3 Catching Efficiencies

Results from three calculations are shown for the smaller MVD of 20 μm:

1. Eulerian (Droplerian), 1 droplet bin (MVD)
2. Eulerian (Droplerian), 10 droplet bins
3. Lagrangian (2FOIL-ICE), 10 droplet bins

The catching efficiencies resulting from these calculations are shown in Fig. 7.

Considering Fig. 7a, it is observed that compared to a mono-disperse droplet disribution the use of a multi-disperse droplet distribution improves the prediction of the catching efficiency. The "tails" of the catching efficiency distribution become more smooth. However, the use of a multi-disperse distribution gives an under prediction around the leading edge.

Figure 7b shows the comparison between the multi-disperse Lagrangian and Eulerian calculation. The results are similar, although again the Eulerian results show an under-prediction compared to the experimental and Lagrangian results.

For the larger 236 μm MVD, representing an SLD case, results of the Lagrangian method are not shown, since the splashing model described in section 3.2 was only implemented in the Eulerian method. The shown results are:

(a) 20 μm MVD

(b) 236 μm MVD
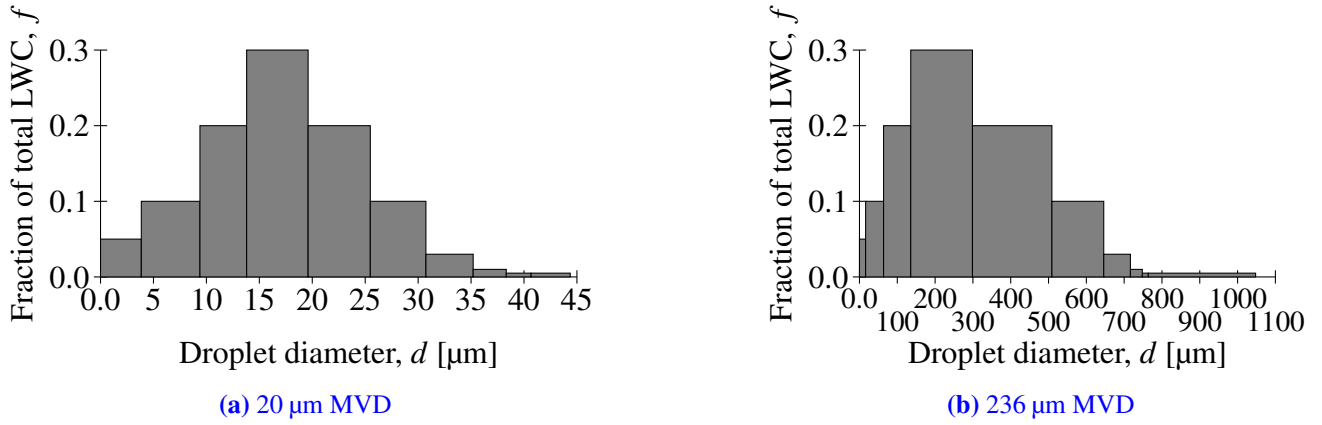
Fig. 5 10-Bin droplet distributions used in simulations
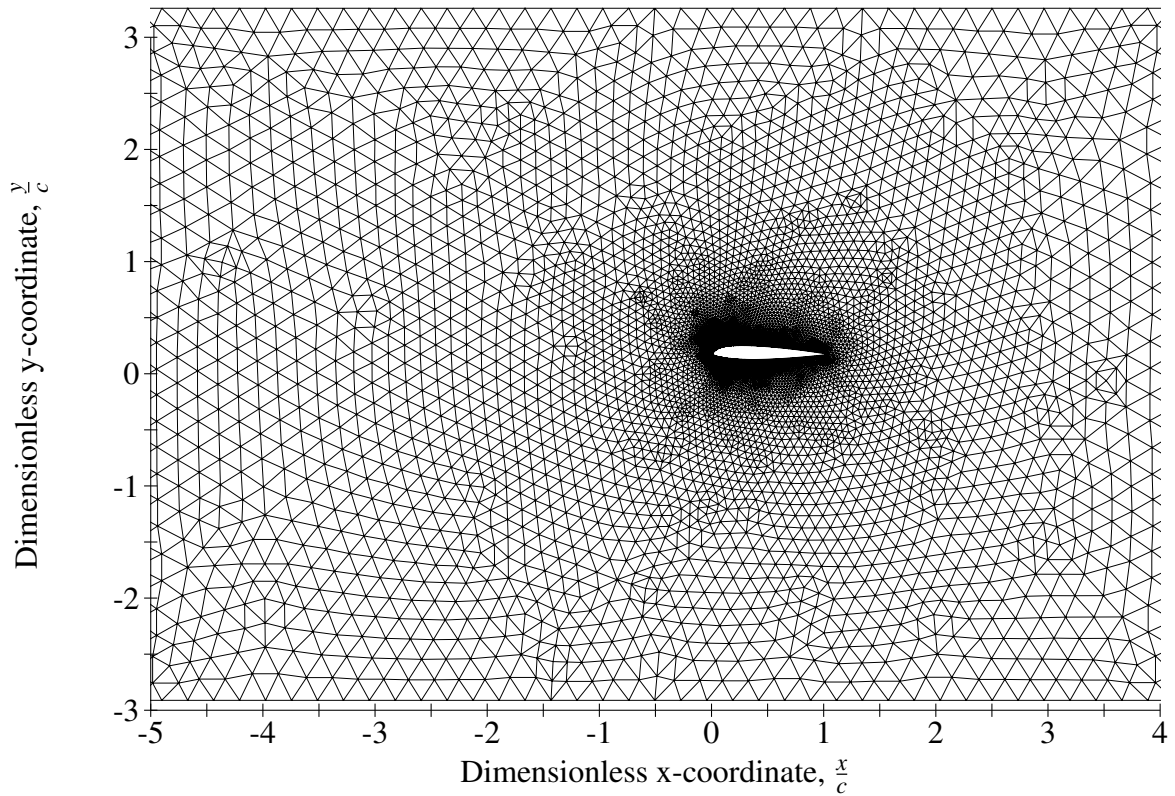
Fig. 6 NACA-23012 mesh used for Eulerian computations
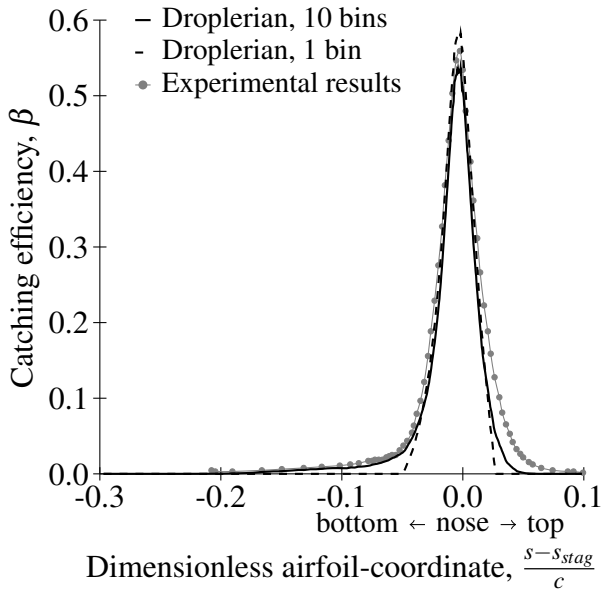
(a) Droplet distribution effects
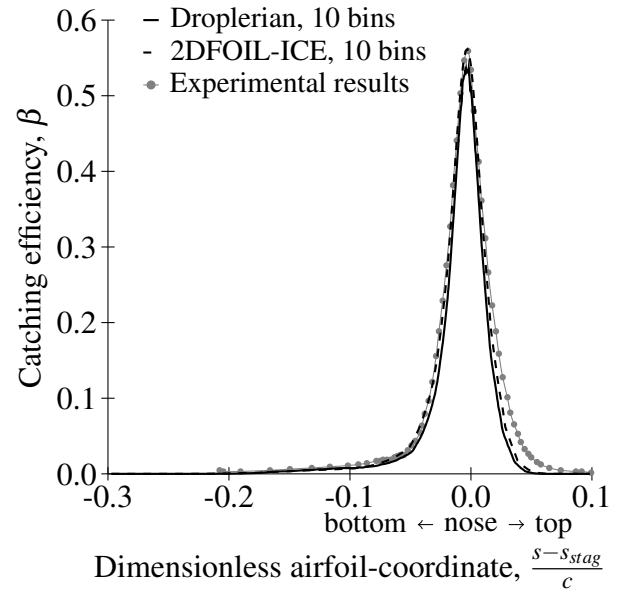
(b) Eulerian (Droplerian) and Lagrangian (2DFOIL) results

Fig. 7 Calculated catching efficiencies, 20 μm MVD, NACA-23012, $AoA = 2.5°$

1. Eulerian, 1 droplet bin (MVD)

2. Eulerian, 10 droplet bins, no splashing

3. Eulerian, 10 droplet bins, splashing

The resulting distributions of the catching efficiencies are shown in Fig. 8.

Again, considering the comparison between the use of mono-disperse and multi-disperse droplet distributions in Fig. 8a an improvement can be seen when the mono-disperse distribution is compared to the multi-disperse droplet distribution. However, the improvement is less significant than for the 20 μm MVD case. Compared to the experimental results, a substantial over-prediction of the catching efficiencies is still present downstream of the leading edge, while around the leading edge an under-prediction is present as it was for the smaller MVD case.

The addition of the splashing model is a possible improvement due to the amount of mass lost through the mass-loss coefficient (reappearing as secondary droplets). Considering the results presented in Fig. 8b, indeed a decrease of the catching efficiency distribution is observed, especially downstream of the leading edge. However, the

splashing model also leads to a decrease in the already under-predicted catching efficiency around the leading edge. Despite this problem, the addition of a splashing model gives a significant improvement in the prediction of the catching efficiency distribution when comparing the results with the experimental results.

5.4 Flow Field

One of the advantages of the Eulerian method is that the droplet velocities and local liquid water content are known everywhere in the computational domain. The entire field can be examined, making it possible to locate the major differences between the results. This is especially useful for the 236 μm MVD case, for which the splashing is more significant.

The most striking result from this comparison is that for the larger droplet diameters (bin 3–10) no visible difference is observed between the results with and without splashing. To illustrate this, the distributions of the local liquid water contents for the largest droplet bin (bin 10, 1046 μm) are shown in Fig. 9.

With or without splashing, all droplets of the larger diameters impinging on the airfoil sur-

(a) Droplet distribution effects

(b) Splashing model effects
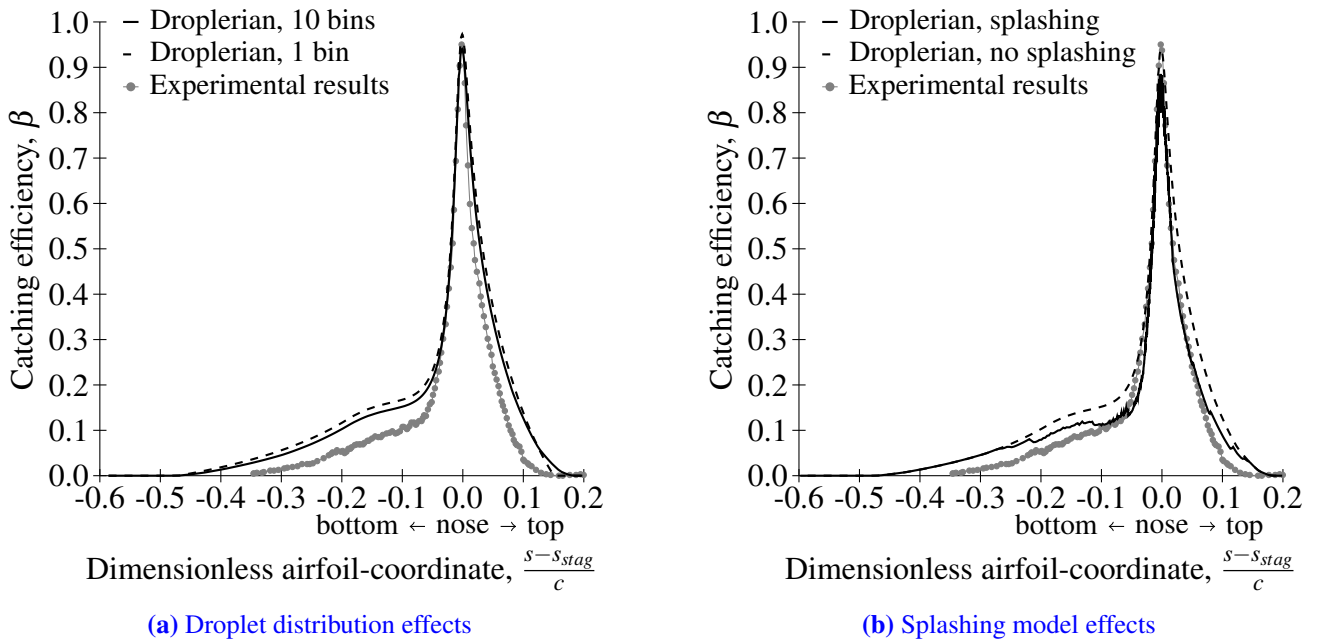
Fig. 8 Calculated catching efficiencies, 236 µm MVD, NACA-23012, $AoA = 2.5°$

(a) Splashing model not active

(b) Splashing model active
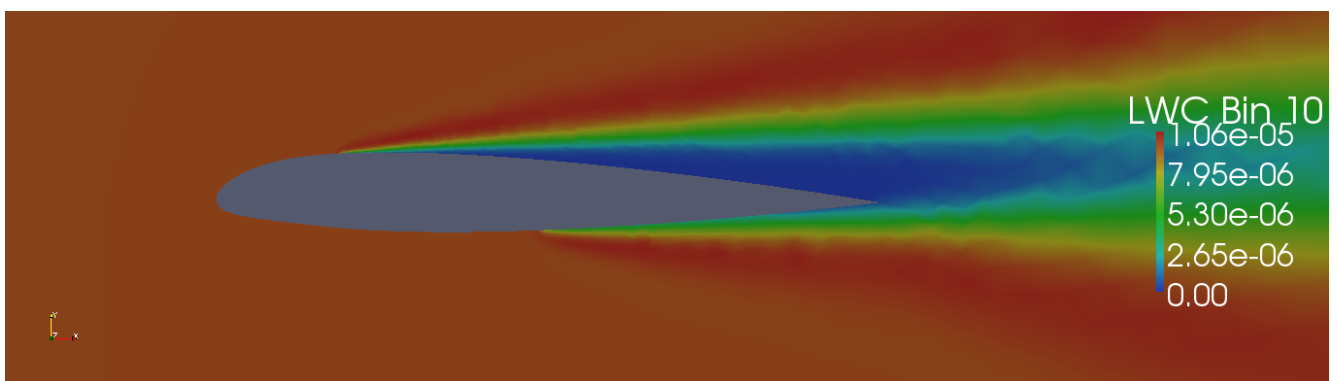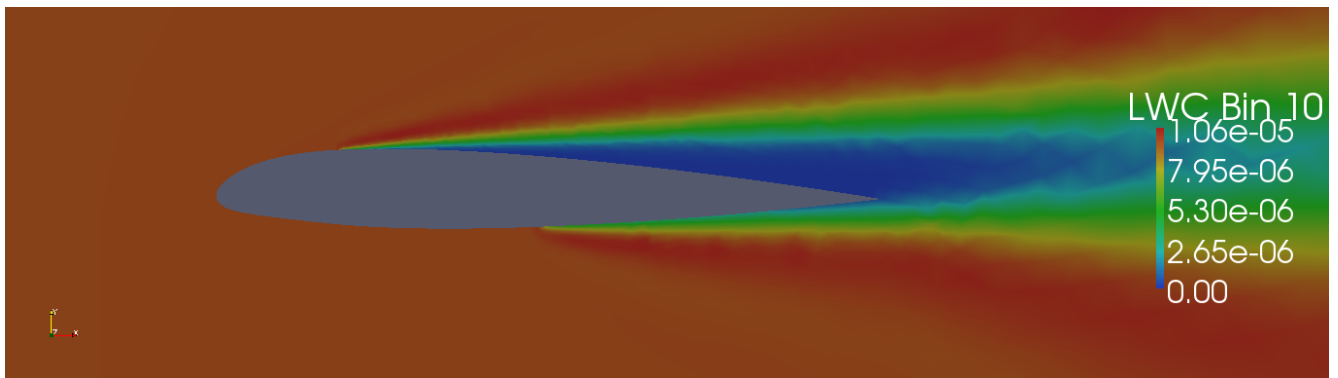
Fig. 9 Calculated droplet density, ρ_d [kg/m^3], 236 µm MVD, bin 10 (1046 µm), NACA-23012, $AoA = 2.5°$

face are extracted from the domain. When the splashing model is *active* (Fig. 9b) the secondary droplets created by a splashing event are re-injected, but in a droplet bin with a smaller diameter.

The droplet velocities are also the same for the results with and without the splashing model, so only one velocity field is shown in Fig. 10. The white lines are droplet trajectories that can be calculated using the droplet velocity field.

Due to the splashing, the major differences can be found for the smallest bins (bin 1 and 2), in which the secondary droplets are apparently re-injected. Figure 11 shows the local liquid water contents for bin 1 (16 μm). With the splashing model *active* (Fig. 11b), an increase in liquid water content can be seen, especially in the areas just downstream of the leading edge.

The small secondary droplets are transported away from the airfoil surface. This is responsible for the lower catching efficiency distribution when the splashing model is active as observed in Fig. 8b.

6 Conclusions

A detailed analysis of the droplet forces has been performed. The assumption that the drag and, to a lesser extend, the buoyancy forces are the dominant forces appears to be valid, although for larger droplets the Basset history force becomes more important. The effect of the inclusion of additional force terms in the calculation of the droplet trajectories is minimal, while the impact on calculation time is large.

An Eulerian method to calculate ice-accretions on two dimensional airfoils has been developed. The method was based on and compared with a similar Lagrangian method, which produced satisfactory results for small droplet diameters. For larger (SLD) droplets the catching efficiency is over predicted. To improve the matching with experimental catching efficiency data, a splashing model has been added to the Eulerian method. Splashing is accounted for by introducing a mass-loss-coefficient and by re-injecting secondary droplets into the droplet

bin corresponding to the diameter closest to the secondary droplet diameter obtained from the splashing model. The inclusion of a splashing model accounts for a decrease in the catching efficiency on the airfoil, bringing the catching efficiency prediction closer to experimental results. This is a clear improvement compared to the case for which splashing was not accounted for. Due to the decreased catching efficiency a smaller ice-accretion is formed around the leading edge of the considered airfoil.

The experimentally and numerically calculated catching efficiencies still differ, which is possibly caused by effects due to rebound and breakup. Models for these effects are considered for future improvements to the method. Improved prediction of the flow around the airfoil, by using more advanced flow-models instead of the currently applied potential-flow-model, might also improve the results.

7 Acknowledgements

References

[1] Cossali G. E, Coghe A, and Marengo M. The impact of a single drop on a wetted solid surface. *Experiments in Fluids*, Vol. 22, No 6, pp 463–472, April 1997.

[2] Dillingh J. E and Hoeijmakers H. W. M. Simulation of ice accretion on airfoils during flight. *Proc FAA In-Flight Icing/Ground De-Icing International Conference & Exhibition*, Chicago, IL, June 2003. 12 pages.

[3] Dillingh J. E and Hoeijmakers H. W. M. Numerical simulation of airfoil ice accretion and thermal
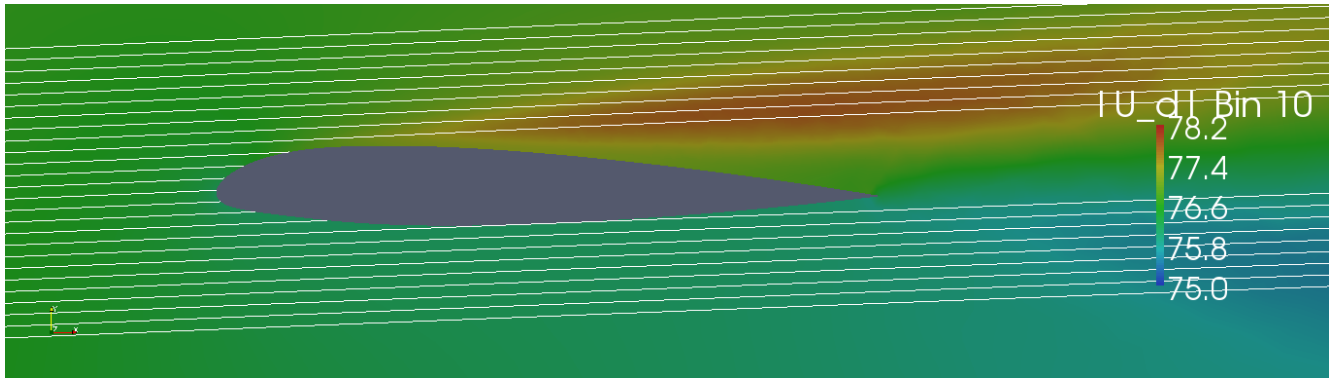
Fig. 10 Calculated droplet velocity, $\left|\vec{U}_d\right|$ [m/s], with calculated droplet trajectories, 236 μm MVD, bin 10 (1046 μm), NACA-23012, $AoA = 2.5°$
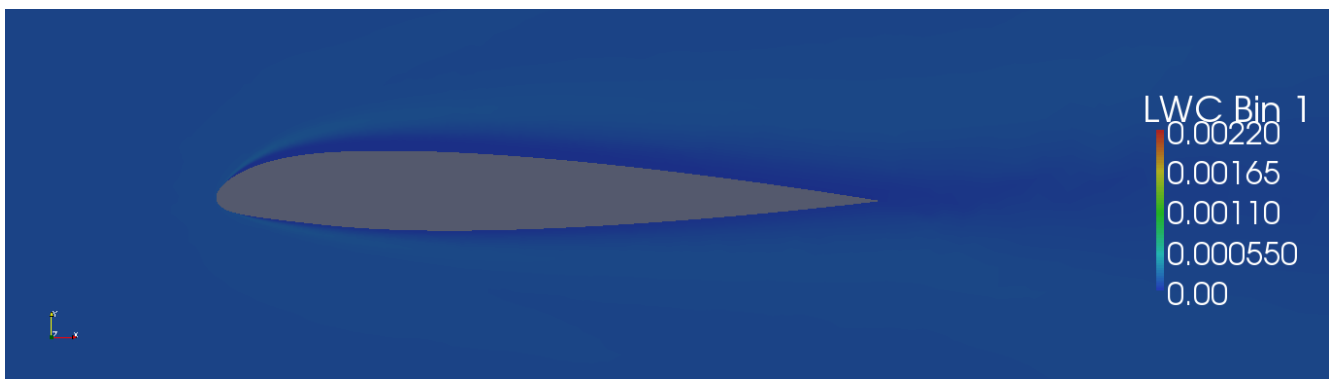
(a) Splashing model not active

(b) Splashing model active

Fig. 11 Calculated droplet density, ρ_d [kg/m^3], 236 μm MVD, bin 1 (16 μm), NACA-23012, $AoA = 2.5°$

anti-icing systems. *Proc ICAS 2004*, Yokohama, Japan, August-September 2004.

[4] Honsek R, Habashi W. G, and Aubé M. S. Eulerian modeling of in-flight icing due to super-cooled large droplets. *Journal of Aircraft*, Vol. 45, No 4, pp 1290–1296, July-August 2008.

[5] Jacobs S. J, Hospers J. M, and Hoeijmakers H. W. M. Numerical simulation of ice accretion on multiple-element airfoil sections. *Proc ICAS 2008*, Anchorage, AK, September 2008.

[6] Kelleners P. H. *An edge-based finite volume method for inviscid compressible flow with condensation*. PhD thesis, University of Twente, Enschede, the Netherlands, December 2007.

[7] Koop A. H. *Numerical simulation of unsteady three-dimensional sheet cavitation*. PhD thesis, University of Twente, Enschede, the Netherlands, September 2008.

[8] Langmuir I and Blodgett K. B. A mathematical investigation of water droplet trajectories. Technical Report 5418, US Army Air Forces, 1946.

[9] Mei R, Lawrence C. J, and Adrian R. J. Unsteady drag on a sphere at finite reynolds-number with small fluctuations in the free-stream velocity. *Journal of Fluid Mechanics*, Vol. 233, pp 613–631, 1991.

[10] Papadakis M, Rachman A, Wong S.-C, Yeong H.-W, Hung K. E, Vu G. T, and Bidwell C. S. Water droplet impingement on simulated glaze, mixed and rime ice accretions. Technical Report NASA/TM-2007-213961, NASA, October 2007.

[11] Petty K. R and Floyd C. D. J. A statistical review of aviation airframe icing accidents in the us. *Proc 11th Conference on Aviation, Range, and Aerospace*, Hyannis, MA, October 2004.

[12] Snellen M. Ice accretion during flight. memorandum m-749. Technical report, Department of Aerospace Engineering, Delft University of Technology, Delft, The Netherlands, 1996.

[13] Snellen M, Boelens O. J, and Hoeijmakers H. W. M. A computational method for numerically simulating ice accretion. *Proc 15th AIAA Applied Aerodynamics Conference*, Atlanta, GA, June 1997. Technical Papers pt 2.

[14] Trujillo M. F, Mathews W. S, Lee C. F, and Peters J. F. Modelling and experiment of impingement and atomization of a liquid spray on a wall. *International Journal of Engine Research*, Vol. 1,

No 1, pp 87–105, 2000.

[15] van Eijkeren D. F and Hoeijmakers H. W. M. Influence of the history term in a lagrangian method for oil-water separation. *Proc 7th International Conference on Multiphase Flow*, Tampa, FL, 2010.

[16] Wright W. B and Potapczuk M. G. Semi-empirical modelling of sld physics. *Proc 42nd AIAA Aerospace Sciences Meeting and Exhibit*, Reno, NV, January 2004.

[17] Yarin A. L and Weiss D. A. Impact of drops on solid surfaces: self-similar capilary waves, and splashing as a new type of kinematic discontinuity. *Journal of Fluid Mechanics*, Vol. 283, pp 141–173, January 1995.

Copyright Statement